ADVANCED MATERIALS
www.advmat.de

Hydrogen Storage in Magnesium Hydride at Room Temperature Enabled by Graphene-Stabilized Multivalent Niobium Oxides

Chaoqun Li, Ying Ding, Xiaoyue Zhang, Xuechun Hu, Xuebin Yu, Dalin Sun, and Guanglin Xia**

Reversible hydrogen storage in magnesium hydride (MgH_2) remains hindered by intrinsic, complicated kinetic barriers associated with both hydrogen release and uptake, particularly under mild conditions. In this work, graphene-confined, low-crystallinity niobium oxide nanoparticles are developed to optimize the kinetic barriers across all stages of hydrogen absorption and desorption in MgH_2. This is realized by the synergistic effect of in situ-generated stable multivalent niobium oxide (NbO_x) and the electronically modulating graphene. It is theoretically and experimentally demonstrated that Nb^{2+} enhances H_2 dissociation and diffusion, while Nb^{4+} facilitates Mg—H bond cleavage and recombination of H_2. Graphene serves a dual function by modulating the electronic environment at NbO_x interfaces to facilitate charge transfer, while confining nanoparticles to prevent aggregation and hence maintain the catalytic stability of NbO_x. Moreover, graphene suppresses the excessive hydrogen binding tendency of over-reduced Nb^0, which otherwise traps H and impedes hydrogen diffusion. This integrated structure ensures the stabilization of active Nb species and lowers energy barriers across all key steps of hydrogen storage. As a result, an effective hydrogen absorption even at 0 °C and an onset hydrogen desorption temperature of 155.9 °C is realized. This provides a versatile strategy for engineering multivalent oxides for promoting hydrogen storage of MgH_2.

1. Introduction

Hydrogen energy, as a clean, efficient, and renewable energy carrier, has received widespread attention driven by the pursuit of carbon neutrality.[1,2] However, the lack of a safe and effective hydrogen storage technique hinders the widespread application of hydrogen energy. Compared to gaseous and liquid hydrogen storage technologies, solid-state hydrogen storage is considered one of the most promising methods due to its high volumetric hydrogen storage density, good safety, and controllable hydrogen release properties.[3–5] Among them, magnesium hydride (MgH_2) has attracted significant attention due to its high hydrogen storage capacity (7.6 wt.%), abundant resource availability, and low cost.[6–8] However, its practical application is limited by two major factors, namely the high enthalpy changes of dehydrogenation (75 $kJ \cdot mol^{-1}$ H_2), which leads to an elevated dehydrogenation temperature. And the slow hydrogenation/dehydrogenation kinetics hinder the rate of hydrogen storage and release. These issues make it difficult for MgH_2 to achieve fast and reversible hydrogen storage at low temperatures. In this context, enabling hydrogen absorption at room temperature or even subzero conditions is particularly desirable, as it can significantly reduce energy consumption, simplify system design, improve safety, and facilitate integration with low-temperature polymer electrolyte membrane fuel cells (PEMFCs) and other energy-efficient technologies.[9]

The hydrogen desorption of MgH_2 involves the cleavage of Mg—H bonds and the combination of hydrogen toward the formation of H_2[10] and its reversible hydrogen absorption of Mg involves three sequential steps: hydrogen molecule dissociation, surface adsorption/migration, and bulk diffusion.[11] While the endothermic dehydrogenation process inherently requires energy input, the exothermic hydrogenation reaction should theoretically proceed spontaneously at ambient conditions. However, high kinetic barriers force hydrogenation to occur at elevated temperatures of over 200 °C, incurring substantial energy penalties. Addressing these kinetic limitations to enable room-temperature or subzero hydrogen absorption represents a critical pathway toward energy-efficient cyclic operation.[12] Previous studies identify hydrogen dissociation as the rate-determining step due to its high activation barrier.[13] Notably, transition metal doping[14] (e.g., V, Ti) and metal oxide additives[15] (e.g., Nb_2O_5) have demonstrated remarkable efficacy in reducing dissociation barriers to near-zero levels. Among these additives, Nb_2O_5 exhibits superior catalytic performance, attributed to the formation of multivalent metal oxides enabled by its low thermal stability, thereby imparting a strong

C. Li, Y. Ding, X. Zhang, X. Hu, X. Yu, D. Sun, G. Xia
College of Smart Materials and Future Energy
Fudan University
Shanghai 200433, China
E-mail: yuxuebin@fudan.edu.cn; xiaguanglin@fudan.edu.cn

The ORCID identification number(s) for the author(s) of this article can be found under https://doi.org/10.1002/adma.202511759

DOI: 10.1002/adma.202511759

affinity for hydrogen.[16–18] During the hydrogen storage reaction, the formation of multivalent Nb species,[19] possessing distinct *d*-electron configurations,[15,20] facilitates electron transfer between Mg and H. Furthermore, metal oxides act as lubricants during ball milling, preserving MgH_2 surface reactivity and improving dehydrogenation kinetics.[21] However, the application of Nb_2O_5 in MgH_2 systems still faces several challenges that hinder further performance enhancement. First, the overly strong hydrogen adsorption on the catalyst surface impedes the subsequent diffusion of hydrogen into the Mg matrix, leading to the presence of a high kinetic barrier for hydrogen adsorption.[22] Second, the rapid reduction of metal oxides under operating conditions compromises the long-term catalytic stability.[23] More importantly, the excessive reduction of Nb-based catalysts leads to the attenuation of the catalytic effect in reducing the kinetic barrier for hydrogen desorption, resulting in an increased operating temperature.[16,18,24] Therefore, although multivalent Nb-based catalysts play an effective role in enhancing hydrogen storage performance of MgH_2, it is still difficult to realize barrierless H_2 dissociation and simultaneously improve reversible hydrogen desorption, and the mechanism behind tuning the catalytic role of multivalent Nb species remains insufficiently understood.

In this work, we engineer a graphene-encapsulated low-crystallinity niobium oxide nanocomposite (denoted as Nb_2O_5@G) to concurrently address the kinetic constraints of dehydrogenation and hydrogenation in MgH_2. Owing to the strong reducing capability of Mg/MgH_2, Nb_2O_5 is prone to form low-valence NbO_x. Compared to Ti-based catalysts (Ti^{3+} or Ti^{2+}) reported in recent studies,[25–27] which utilize a single dominant valence state to mediate hydrogen absorption and desorption, the thus-formed multi-valent Nb species (Nb^{5+}, Nb^{4+}, and Nb^{2+}) form Nb_2O_5@G plays a synergistic effect in various hydrogenation and dehydrogenation steps. It is theoretically demonstrated that low-valence NbO_x with various valences plays different roles in alleviating the kinetic barriers of MgH_2. Among them, Nb^{2+} and Nb^{4+} containing oxides exhibit the best catalytic effect in promoting H_2 dissociation and diffusion into Mg and H_2 adsorption, respectively, and NbO_2 exhibits a superior catalytic effect in promoting the cleavage of Mg—H bonds and the combination of hydrogen toward the formation of H_2. However, the formation of Nb^0 through excessive reduction results in the favorable H_2 dissociation via spin-polarized charge transfer into the H_2 σ^* antibonding orbital, which leads to the formation of overly stable Nb—H bonds and ultimately hinders hydrogen diffusion into Mg. Interestingly, Nb^{4+} and Nb^{2+} containing oxides and Nb^0 are in situ formed and well-preserved during hydrogen storage of MgH_2 under the catalysis of Nb_2O_5@G. Moreover, the introduction of graphene reduces the magnetic moment of Nb_2 from 2.0 μ_B to 0.0 μ_B, which alleviates the excessive hydrogen adsorption of Nb^0, and simultaneously leads to the formation of electron-rich regions at the interfaces between graphene and Nb of NbO_x induced by the graphene's π-electron contribution, which creates electron-accepting orbitals compatible with H_2 σ^* orbitals and hence lowers the H_2 dissociation barrier. In addition, the introduction of graphene matrix not only modulates the electronic structure at the catalyst interface but also physically confines NbO_x nanoparticles to prevent aggregation and stabilize multivalent Nb species. Therefore, all the kinetic barriers involved during reversible hydrogen absorption and desorption of MgH_2 are well alleviated under the catalysis of Nb_2O_5@G, which enables instant hydrogenation at ambient temperature (25 °C) and even facilitates hydrogen uptake even at 0 °C and an onset hydrogen desorption temperature of 155.9 °C, offering practical advantages for the application of MgH_2 in low-temperature environments.

2. Results and Discussion

2.1. Synthesis and Characterization of Nb_2O_5@G

The synthesis process for Nb_2O_5@G is illustrated in **Figure 1a**, achieved through a straightforward sequence of heating with stirring, freeze-drying, and subsequent high-temperature calcination. X-ray diffraction (XRD) pattern displays diffraction peaks at 22.6°, 28.4°, 36.6°, 46.2°, and 55.1°, which closely align with the standard Nb_2O_5 reference (PDF#30-0873)[28] (Figure 1b). To validate the phase, Nb_2O_5@G was recrystallized at 800 °C under Ar. The resulting XRD pattern shows sharper peaks matching the original, confirming the presence of low-crystallinity Nb_2O_5. The observed weak peaks indicate Nb_2O_5 exists with small particle sizes and low crystallinity. Scanning electron microscopy (SEM) confirms the distribution of Nb_2O_5 nanoparticles with diameters <15 nm across the crumpled graphene surface, in which graphene plays a supporting role in preserving the structural integrity of Nb_2O_5@G (Figure 1c). Energy-dispersive spectroscopy (EDS) mapping demonstrates the uniform dispersion of Nb and C, confirming the homogeneous distribution of Nb_2O_5 particles on the graphene surface (Figure S1, Supporting Information). After the thermal reduction of graphene oxide during the synthesis, Raman spectroscopy (Figure S2a, Supporting Information) showed an I_D/I_G ratio of 1.1, indicating moderately defective reduced graphene oxide. Thermogravimetry (TG) analysis (Figure S2b, Supporting Information) further confirmed that graphene accounted for ≈27.5 wt.% of the composite. High-resolution TEM (HRTEM) further reveals a lattice spacing of 0.393 nm, corresponding to the (001) plane of Nb_2O_5 (Figure 1d), which is consistent with XRD results. Additionally, X-ray photoelectron spectroscopy (XPS) analysis of Nb_2O_5@G shows a Nb 3*d* doublet at 207.3 and 210.0 eV,[29] which provides additional evidence for the formation of Nb_2O_5 (Figure 1e). These characterization results indicate the successful preparation of Nb_2O_5 nanoparticles supported on the graphene surface. For comparison, the calcined bare Nb_2O_5 (nano-Nb_2O_5) exhibits micron-sized agglomerates due to graphene decomposition during heating, resulting in sharper XRD peaks than those of Nb_2O_5@G, while the commercial Nb_2O_5 particles (C-Nb_2O_5) show larger sizes with irregular morphologies (Figure S3, Supporting Information). After mechanical ball-milling with MgH_2, adding 10 wt.% Nb_2O_5@G, the thus-obtained Nb_2O_5@G-MgH_2 composite demonstrates a homogeneous spatial distribution of Mg, Nb, and C throughout the sample, directly confirming uniform integration of Nb_2O_5@G into the MgH_2 matrix (Figure 1f).

2.2. Hydrogen Storage Performance of Nb_2O_5@G-MgH_2

The hydrogen desorption performance of MgH_2 under the catalysis of 10 wt.% Nb_2O_5@G is assessed first. Temperature-

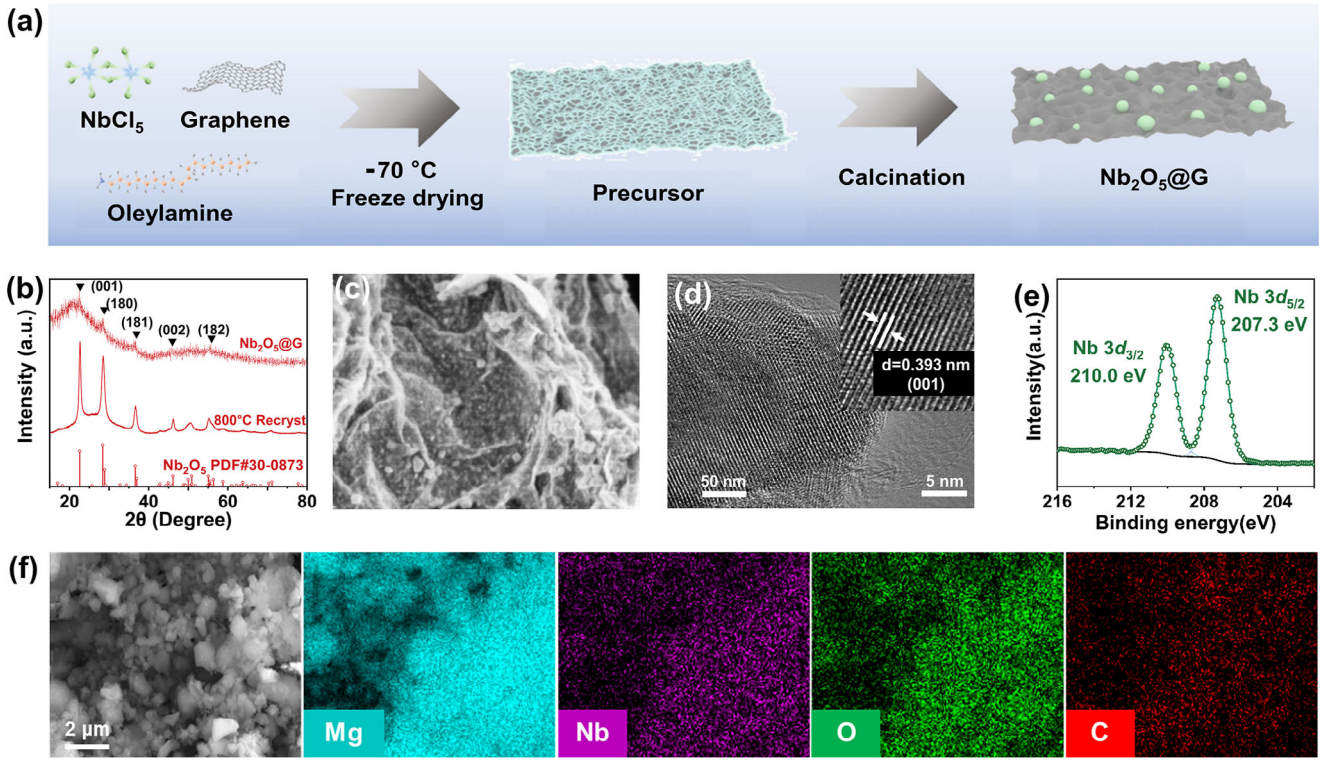

Figure 1. a) Schematic illustration of the synthesis process of Nb_2O_5@G. b) XRD patterns, c) SEM, d) HRTEM images, and e) high-resolution Nb 3*d* XPS spectra of Nb_2O_5@G. f) SEM-EDS elemental mapping images of Mg, Nb, O, and C of Nb_2O_5@G-MgH_2.

programmed desorption (TPD) curves during the initial dehydrogenation demonstrate that MgH_2 catalyzed by Nb_2O_5@G begins to release H_2 at 208.9 °C and reaches a dehydrogenation peak at 230.9 °C, which are 96.0 and 96.6 °C lower than those of ball-milled MgH_2, respectively (**Figure** 2a). To quantitatively describe the effect of Nb_2O_5@G in enhancing the H_2 desorption kinetic performance of MgH_2, the activation energy (E_a) was calculated by the Kissinger method (Figure S4, Supporting Information). The fitting results show that the dehydrogenation activation energy of Nb_2O_5@G-MgH_2 is significantly reduced to 92.3 kJ mol^{-1} H_2, demonstrating a 31.5% reduction compared to the 134.7 kJ mol^{-1} H_2 of ball-milled MgH_2 (Figure S5, Supporting Information). It is worth noting that MgH_2 catalyzed by nano-Nb_2O_5 without the presence of graphene also exhibits similar H_2 release performance, with a significant reduction in dehydrogenation temperature compared to MgH_2 catalyzed by commercial Nb_2O_5 (C-Nb_2O_5). These results highlight the critical role of nanoscale Nb_2O_5 in enhancing the dehydrogenation performance of MgH_2.

Notably, compared to the initial dehydrogenation process, the secondary H_2 desorption curves of various samples exhibited varying degrees of alteration (Figure S6, Supporting Information). Specifically, MgH_2 catalyzed by Nb_2O_5@G exhibits a remarkable reduction in onset temperature from 208.9 to 155.9 °C, and the final H_2 desorption temperature decreases from 272.2 to 243.6 °C (Figure 2b). This suggests that the active catalytic species undergo phase changes after the initial H_2 desorption, attributed to the high reducibility of MgH_2 and Mg, leading to exceptional dehydrogenation performance in the second cycle compared to the initial process and minimal degradation in H_2 capacity, which could also be evidenced by previous literature.[30,31] The newly evolved catalytic species further reduce the apparent activation energy for MgH_2 dehydrogenation to 78.1 kJ·mol^{-1} (Figure S7, Supporting Information). Interestingly, MgH_2 catalyzed by nano-Nb_2O_5 also maintained stable H_2 desorption capacity, but with the secondary H_2 desorption temperature 10–50 °C higher than that of MgH_2 catalyzed by Nb_2O_5@G from the onset to the end of H_2 desorption process, indicating that graphene plays an important role in maintaining the superior catalytic effect of nano-Nb_2O_5 in improving dehydrogenation performance of MgH_2. In contrast, MgH_2 under the catalysis of C-Nb_2O_5 shows almost no change in H_2 desorption temperature between the initial two dehydrogenation processes, even experiencing a reduction in H_2 capacity from 6.4 to 5.9 wt.% (Figure S6). These results demonstrate that the phase change of Nb_2O_5 promotes its catalytic effect in improving the dehydrogenation performance of MgH_2, which could be well preserved by graphene, while the decrease of particle size in Nb_2O_5@G enhances the phase change reaction of Nb_2O_5.

In addition, isothermal dehydrogenation performance of MgH_2 catalyzed by Nb_2O_5@G after the first cycle of hydrogenation verifies full dehydrogenation of 6.2 wt.% within 5 min at 260 °C (Figure S8, Supporting Information). Remarkably, upon decreasing the temperature to even 200 °C, it still retains 2.6 wt.% H_2 release capacity within 30 min. This further emphasizes the role of the in situ-generated Nb-based catalytic species after the first cycle of dehydrogenation in enabling superior low-temperature dehydrogenation performance.

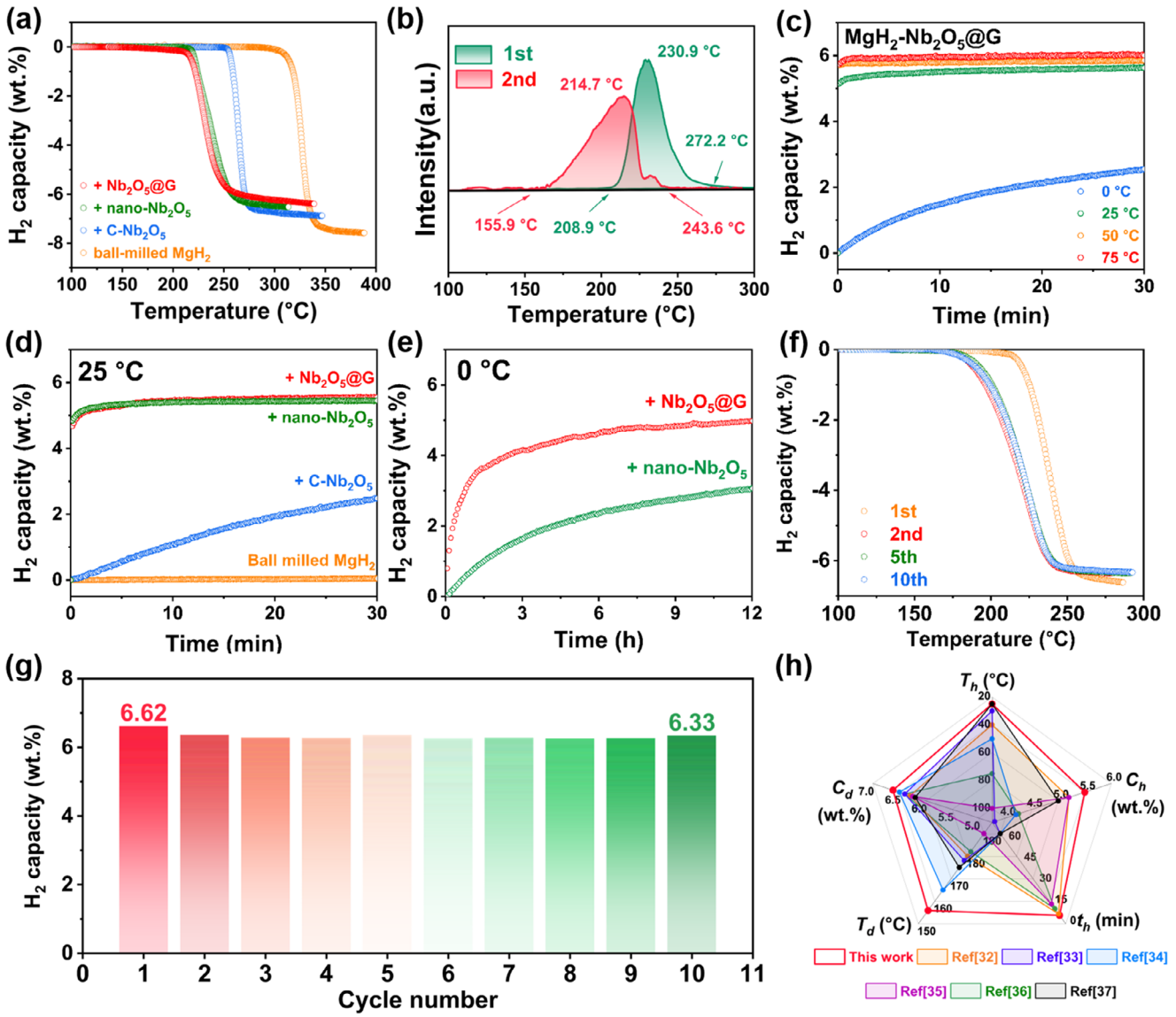

Figure 2. a) TPD results of ball-milled MgH_2 and MgH_2 under the catalysis of Nb_2O_5@G, nano-Nb_2O_5, and commercial Nb_2O_5 (C-Nb_2O_5), respectively. b) The first and second TPD derivative curves of MgH_2 under the catalysis of Nb_2O_5@G. c) Isothermal hydrogenation curves of MgH_2 catalyzed by Nb_2O_5@G at different temperatures. d) Isothermal hydrogenation curves of ball-milled MgH_2 and MgH_2 catalyzed by Nb_2O_5@G, nano-Nb_2O_5, and C-Nb_2O_5 at room temperature (25 °C). e) Isothermal hydrogenation curves of MgH_2 catalyzed by Nb_2O_5@G and nano-Nb_2O_5 at 0 °C. f) TPD results and g) the reversible capacity of MgH_2 catalyzed by Nb_2O_5@G upon cycling. h) Performance comparison of MgH_2-based materials with reported low-temperature hydrogenation systems.[32–37] T_h, t_h, C_h, T_d, and C_d denote hydrogenation temperature, hydrogenation time, hydrogen capacity under T_h and t_h conditions, dehydrogenation onset temperature, and total dehydrogenation capacity, respectively.

The reversible hydrogen absorption performance of MgH_2 catalyzed by Nb_2O_5@G is evaluated subsequently. MgH_2 catalyzed by Nb_2O_5@G exhibits near-instantaneous (>4 wt.% hydrogenation within a few seconds) H_2 absorption at both 50 and 75 °C under 50 bar H_2 pressure, with absorption curves leveling off shortly afterward, and the final H_2 uptake capacity reaches 5.6 and 5.8 wt.% within 30 min, respectively (Figure 2c). In contrast, pristine MgH_2 absorbs only 5.0 wt.% H_2 even at a high temperature of 150 °C within 30 min (Figure S9, Supporting Information), highlighting the advantage of Nb_2O_5@G in accelerating the hydrogenation kinetics of MgH_2. It is worth noting that when the hydrogenation temperature is further reduced to room temperature (25 °C), MgH_2 catalyzed by Nb_2O_5@G could still instantaneously absorb 5.0 wt.% H_2 within 1 min (Figure 2d). For comparison, pure Mg is unable to absorb H_2 at this temperature, and Mg catalyzed by C-Nb_2O_5 exhibits a gradual H_2 uptake, reaching a capacity of only 2.5 wt.% within 30 min. Additionally, Mg catalyzed by nano-Nb_2O_5 displays similarly excellent hydrogenation performance, with its H_2 absorption curve closely resembling that of Nb_2O_5@G, which emphasizes the importance of the nanoscale size of Nb_2O_5 in enhancing the low-temperature hydrogenation performance of Mg. Furthermore, even under a low hydrogen pressure of 1 bar at room temperature, the Nb_2O_5@G-catalyzed composite could still absorb 3.2 wt.% H_2

within 30 min (Figure S10, Supporting Information). In addition to low-pressure hydrogenation, the catalyst also exhibits excellent low-temperature hydrogenation performance, even at an ultralow temperature of 0 °C, Mg catalyzed by nano-Nb_2O_5 and Nb_2O_5@G still demonstrates considerable hydrogenation capacity, and Mg under the catalysis of Nb_2O_5@G exhibits a faster H_2 absorption rate during the first 2 h, as shown in Figure 2e. Ultimately, Mg catalyzed by Nb_2O_5@G absorbs 5.0 wt.% H_2, whereas only a capacity of 3.0 wt.% H_2 is achieved under the catalysis of nano-Nb_2O_5 after 12 h at 0 °C, further confirming its exceptional catalytic efficiency under practical, mild conditions. Based on the pressure-composition isotherm (PCI) curves of MgH_2 catalyzed by Nb_2O_5@G at different temperatures and the van't Hoff equation (Figure S11, Supporting Information), the enthalpy change (ΔH) for hydrogen desorption of Mg catalyzed by Nb_2O_5@G is calculated as 75.0 ± 1.5 kJ mol^{-1}, which is similar to that of pristine MgH_2 (76.6 ± 1.2 kJ mol^{-1}). This indicates that the incorporation of Nb_2O_5@G demonstrates negligible influence on the thermodynamic properties of the reaction, with its enhancement mechanism principally attributed to kinetic optimization rather than thermodynamic modulation.

Cycling stability is a crucial indicator for evaluating reversible H_2 storage performance of materials, and hence over 10 H_2 absorption-desorption cycles were conducted for Nb_2O_5@G-MgH_2, with each TPD analysis for hydrogen desorption performed at a heating rate of 2 °C min^{-1}. After the initial H_2 desorption, the dehydrogenation temperature of MgH_2 under the catalysis of Nb_2O_5@G further decreases and maintains a stable H_2 desorption temperature and kinetic performance during subsequent cycles (Figure 2f). This result suggests that the gradual enhancement of the catalytic effect of Nb-based catalysts occurs during the continuous hydrogen storage process. The initial H_2 desorption capacity of Nb_2O_5@G-MgH_2 is 6.62 wt.%, while it remains at 6.33 wt.% after 10 cycles, demonstrating excellent reversible H_2 storage performance with a high capacity retention of 95.6% (Figure 2g). To the best of our knowledge, this material represents one of the most promising MgH_2-based candidates for low-temperature hydrogen storage reported to date,[32–37] offering not only exceptional hydrogenation capability at reduced temperatures, but also improved cycling stability and excellent dehydrogenation performance compared with other low-temperature systems (Figure 2h).

2.3. Catalytic Species of Nb_2O_5@G-MgH_2 at Different Stages

To monitor the phase changes of Nb_2O_5@G-MgH_2 during H_2 cycling, XRD analysis was performed. As shown in Figure S12 (Supporting Information), only the Mg phase (PDF#35-0821) after H_2 desorption and the MgH_2 phase (PDF#12-0697) after hydrogen absorption are observed, indicating that the reversible transformation between Mg and MgH_2 accounts for repeated hydrogen storage cycles of Nb_2O_5@G-MgH_2. However, no characteristic diffraction peaks of Nb_2O_5-related phases could be observed due to the intrinsic weak diffraction intensity of Nb_2O_5 nanoparticles with low content.[28] Fortunately, the high-resolution XPS Nb 2*p* spectra show the presence of Nb^{5+}, Nb^{2+}, and Nb^0, indicating that Nb_2O_5 was partially reduced by MgH_2 during the ball-milling process (**Figure 3a**). After the initial H_2 desorption, Nb^{5+} disappears and is completely converted into lower-valence Nb species, including Nb^{4+}, Nb^{2+}, and Nb^0, with the content of Nb^{2+} and Nb^0 further increasing to 76% (Figure 3b). These lower-valence Nb species maintain their states throughout subsequent hydrogen absorption and desorption cycles (Figure S13, Supporting Information). High-resolution TEM (HRTEM) images corroborated this conclusion. In addition to the reversible Mg and MgH_2 phases, lattice fringes corresponding to Nb, NbO_x, and NbH_2 are observed at the states of ball milling, H_2 desorption, and absorption (Figure 3c). Notably, the relative contents of lower-valence Nb species remain stable during cycling, indicating that the active catalytic species stabilize after the initial H_2 desorption cycle (Figure 3b). This aligns with the observed decrease in H_2 desorption temperature (Figure 2b), confirming that the lower-valence niobium oxides and metallic Nb are possibly responsible for enhancing the catalytic activity of Nb_2O_5@G.

In addition, comparative experiments show that the valence-state evolution of Nb varies among different catalysts. As shown in Figure S14 (Supporting Information), although Nb_2O_5 is partially reduced to NbO_x and metallic Nb upon dehydrogenation, a significant portion remains unconverted for MgH_2 catalyzed by both nano-Nb_2O_5 and C-Nb_2O_5. In contrast, the presence of graphene in Nb_2O_5@G facilitates the predominant conversion of Nb_2O_5 to Nb^{4+} and lower-valence states, whereas nanosized and commercial Nb_2O_5 retain over 30% Nb^{5+}. This result directly demonstrates that the decrease of particle size and the uniform distribution of Nb_2O_5 on graphene promotes the reduction of Nb_2O_5 by MgH_2 or Mg and hence the formation of more low-valent Nb-based catalytic species. Meanwhile, graphene preserves a uniform distribution of low-valent Nb-based catalytic species during cycling, contributing to its superior H_2 desorption and absorption performance in subsequent cycles.

2.4. Theoretical Studies on the Catalytic Mechanism of Nb_2O_5@G-MgH_2

In order to unveil the enhanced catalytic mechanism induced by the formation of multivalent Nb-based species, density functional theory (DFT) calculations were conducted using various Nb^0, NbO_x clusters (e.g., Nb_2, NbO, Nb_2O_2, NbO_2, Nb_2O_5), and Nb_2O_5 slab model was cleaved from bulk Nb_2O_5 (b- Nb_2O_5) for theoretical simulation. It is well known that the sluggish kinetics of MgH_2 dehydrogenation largely stem from the high stability of the Mg—H bond, which poses a significant obstacle to hydrogen release.[38–41] As shown in **Figure 4a–d**, NbO_x species on the MgH_2 surface significantly weaken Mg—H bonds, elongating their bond lengths from 1.87 Å in pristine MgH_2 (110) surfaces to 1.90—2.27 Å. This bond elongation reflects a significant reduction in the strength of the Mg—H interaction, facilitated by the formation of interfacial Mg—O and Nb—H bonds. Another critical challenge in the dehydrogenation of MgH_2 is its intrinsically high energy barrier,[42–45] which severely limits hydrogen release kinetics. In order to understand the weakening of Mg—H bonds in facilitating hydrogen desorption kinetic of MgH_2, the energy barrier of the typical two-step mechanism[46] is further calculated, first, the Mg—H bond is cleaved and the dissociated hydrogen atom migrates toward the catalyst surface; second, the recombination of two surface-adsorbed hydrogen atoms occurs

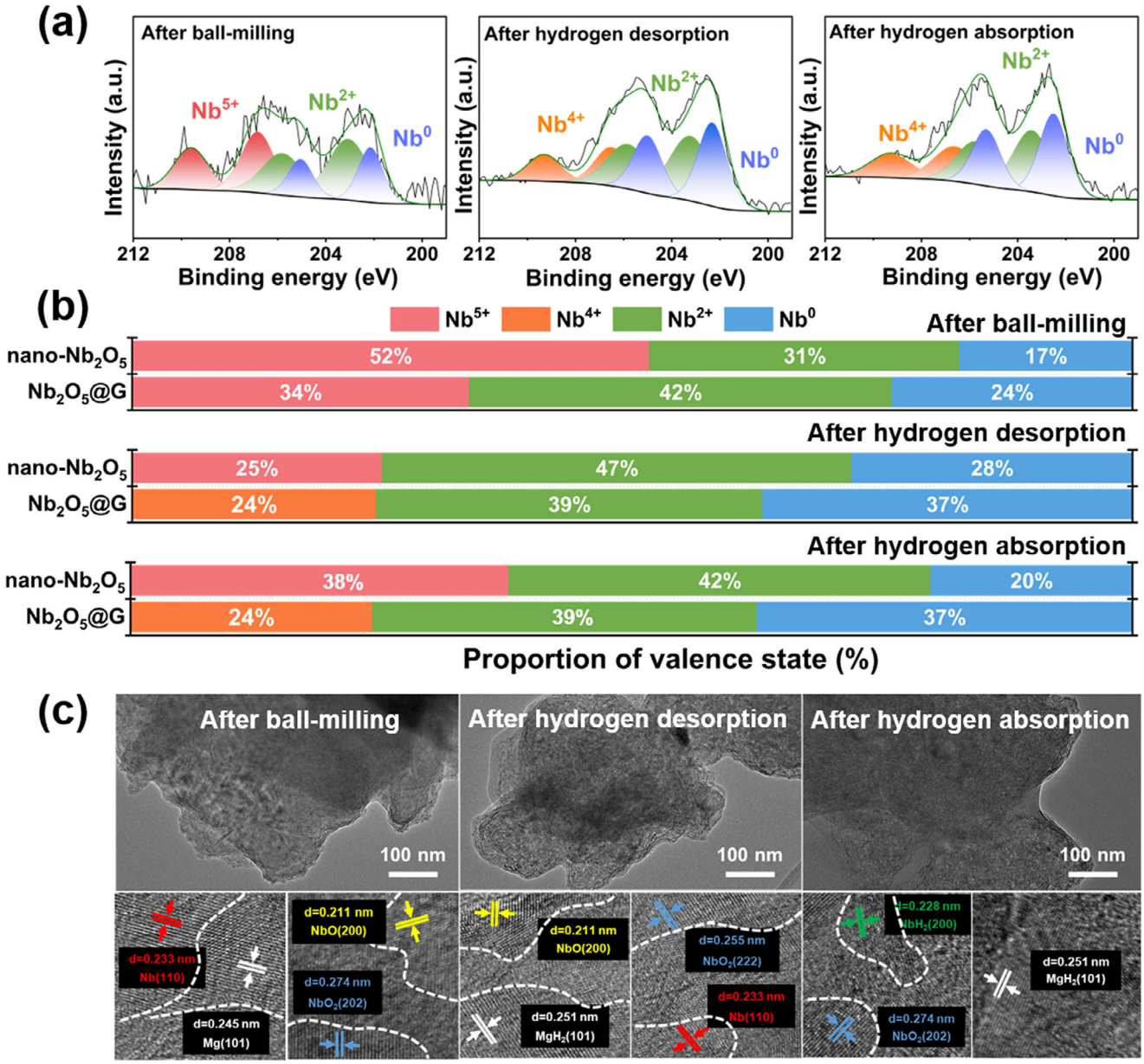

Figure 3. a) Nb 3d XPS spectra of MgH_2 catalyzed by Nb_2O_5@G upon cycling. b) Changes in Nb valence state distribution during hydrogen storage cycling. c) HRTEM images of MgH_2-Nb_2O_5@G after ball-milling, the 1st cycle of hydrogen desorption, and the 1st cycle of hydrogen absorption.

on the NbO_x interface to form H_2. Transition-state (TS) calculations for all systems indicate that the energy barrier for Mg—H bond breaking is substantially reduced and is no longer the rate-determining step. Instead, a high H_2 recombination barrier has been identified as the critical kinetic limitation step (Figure 4e). Remarkably, NbO_2 cluster achieves a low rate-determining barrier of 1.29 eV, far below the dehydrogenation barrier of pristine MgH_2 (2.37 eV). The hierarchy of rate-determining energy barriers across systems (Mg > b-Nb_2O_5 (crystalline) > Nb_2 > Nb_2O_5 (cluster) > NbO > NbO_2) aligns well with the hydrogen desorption performance trends (Figure 2a). As a result, the favorable formation of Nb^{4+} species from Nb_2O_5@G after hydrogen adsorption, as evidenced by experimental results (Figure 3b) is determined to be the key factor that contributes to its outstanding catalytic performance in the hydrogen desorption process than nano-Nb_2O_5.

Notably, Nb_2O_5 clusters induce the substitution of bridge-site H in MgH_2 with O, as shown in Figure 4a and Figure S15 (Supporting Information), suggesting that nanoscale high-valent Nb oxides promote rapid surface oxidation of MgH_2. This also explains the disappearance of Nb^{5+} in the Nb 3*d* XPS spectra exclusively for Nb_2O_5@G (Figure 3a). Without the presence of graphene, the crystallization and aggregation of nanoscale Nb_2O_5 (Figure S16, Supporting Information) hinder the formation of Nb^{4+} species, whereas the presence of Nb^{4+} in MgH_2-Nb_2O_5@G (Figure 3a) has a more favorable dehydrogenation

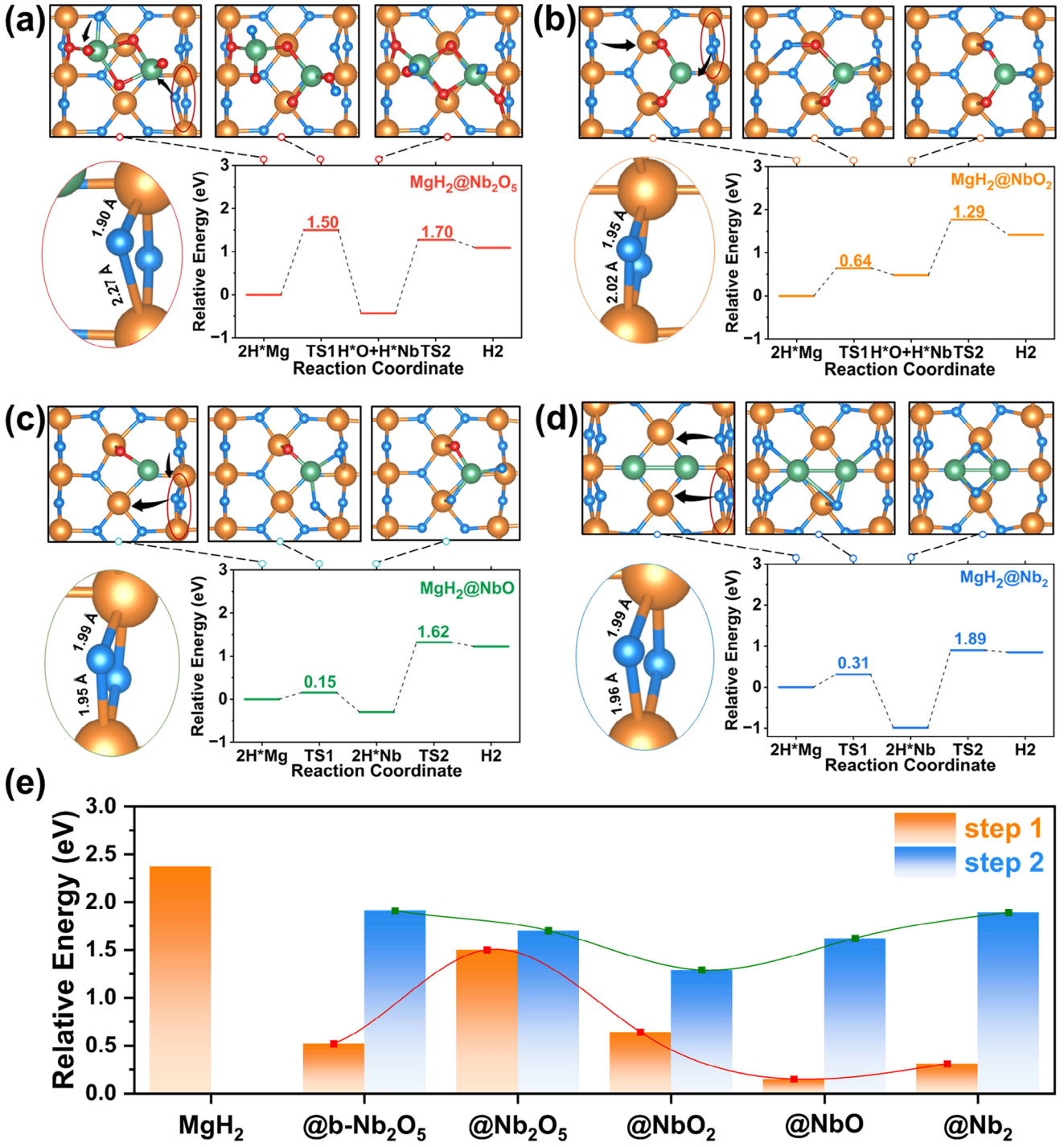

Figure 4. Energetic and structural evolution during the hydrogen desorption process on the MgH_2 (110) surface for MgH_2@Nb_2O_5 a), MgH_2@NbO_2 b), MgH_2@NbO c), and MgH_2@Nb_2 d). e) The comparison of the hydrogen desorption energy barrier on the MgH_2 surface with Nb oxidation states and catalyst particle size.

thermodynamics with a smoother enthalpic transition and a lower H_2 release energy barrier (Figure 4d). Consequently, a significant enhancement in hydrogen desorption performance is observed in the second cycle of hydrogen storage (Figures S6, S7, Supporting Information).

During the reversible hydrogenation of Mg, three critical steps,[25,47] including H_2 dissociation, H adsorption/bonding on the Mg surface, and H diffusion into Mg bulk, are mainly involved. First, the climbing image nudged elastic band (CI-NEB) method was employed to elucidate the energetic and

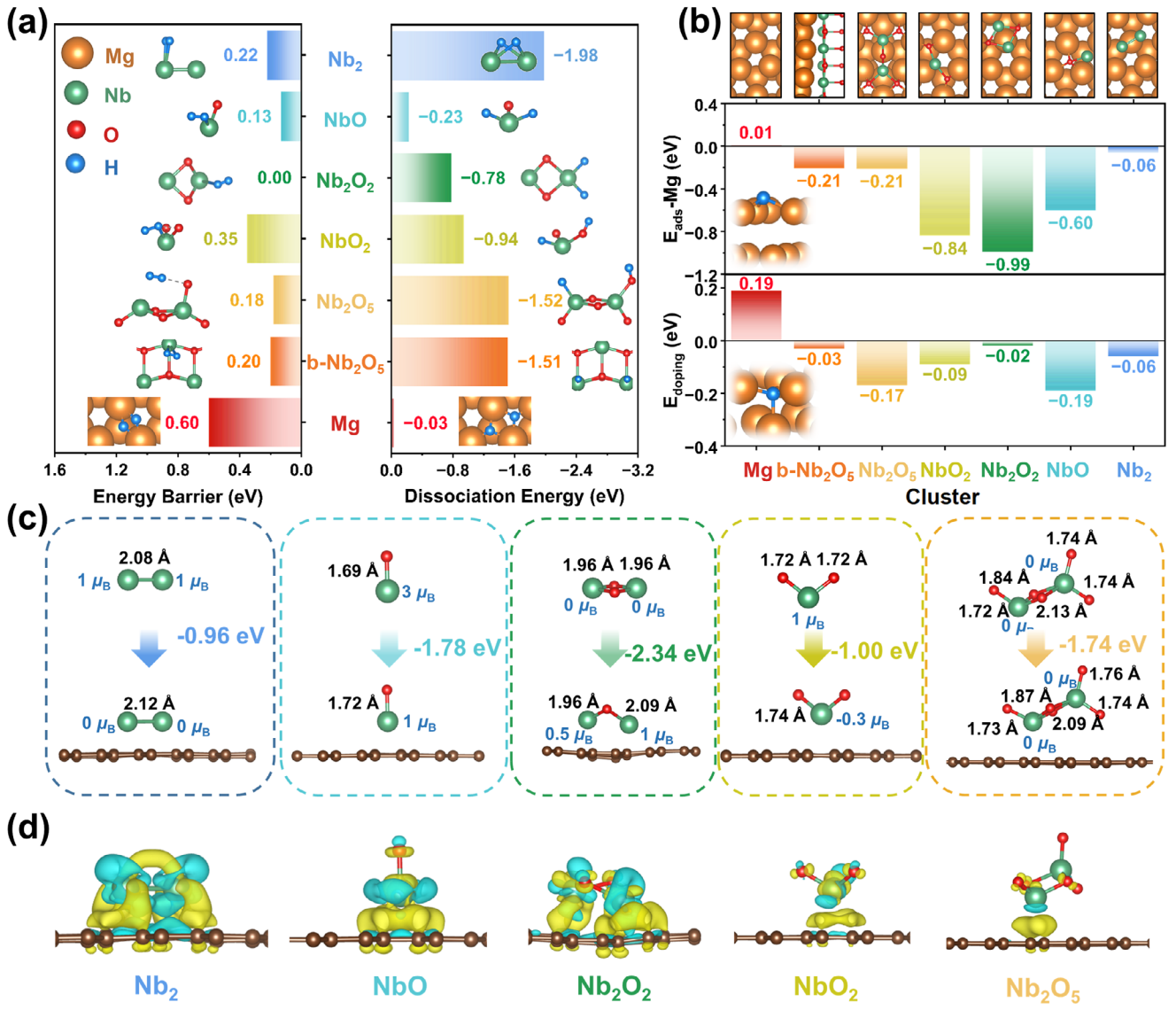

Figure 5. a) Energetic and structural evolution of H_2 dissociation catalyzed by NbO_x@G. Graphene is omitted in the figure for simplicity. The left side illustrates the transition state structure and H_2 dissociation energy barrier, while the right side depicts the final state structure and the energy after H_2 dissociation. b) Structures of different NbO_x@Mg systems and their H adsorption energy (E_{ads}) on Mg surfaces and H interstitial doping energy (E_{doping}) in the bulk. The orange, blue, green, red, and brown spheres represent Mg, H, Nb, O, and C atoms, respectively. c) The ground-state structures of NbO_x and NbO_x@G and the comparison of their Nb atomic magnetic moments and binding energies between NbO_x and graphene. d) The charge density differences of NbO_x@G, where yellow indicates electron accumulation and blue indicates electron depletion. The charge density differences are plotted with an isovalue of 0.005 e·Bohr^{-3}.

structural evolution of the dissociation pathway for both graphene-supported and unsupported NbO_x structures (**Figure** 5a). To achieve low-temperature hydrogenation, a low-barrier H_2 dissociation pathway is essential. The results reveal that Nb-based catalysts exhibit significantly enhanced H_2 dissociation kinetics, with energy barriers reduced by 0.25–0.60 eV compared to the Mg (0001) surface (0.60 eV). Remarkably, the in situ formation of Nb^{2+} during the hydrogen storage of MgH_2 catalyzed by Nb_2O_2@G is able to realize a barrierless H_2 dissociation process (0 eV), which is identified as the key factor responsible for its high hydrogenation activity at 0 °C.

After H_2 dissociation, particular attention was given to the preferential formation of Nb—H bonds and the interaction between Mg and O species during the investigation of hydrogen migration and diffusion behavior. The structural relaxation of NbO_x on the Mg (0001) surface (Figure 5b) indicates that the system maximizes Mg—O interactions. On the Mg surface, Nb_2O_5 clusters adopt a C_{2v}-symmetric configuration through a symmetry transformation, whereas the ground-state structure involved in the MgH_2 dehydrogenation and H_2 dissociation processes exhibits C_s symmetry. This structural evolution promotes stronger interfacial coupling with Mg, which could facilitate the catalytic effect of Nb-based catalysts. Interestingly, induced by the

interaction between Mg and O, the hydrogen adsorption energy on the Mg surface is lower by 0.15–0.57 eV for NbO_x@Mg compared to pristine Mg(0001), and among them, NbO_2 (−0.56 eV) and Nb_2O_2 (−0.40 eV) show the best performance in reducing hydrogen adsorption energy on Mg. The reduced hydrogen adsorption energy on the Mg surface suggests that Mg can more readily capture H from the catalyst interface, thereby accelerating hydrogen diffusion across the Mg surface. Overall, the presence of NbO_x species significantly reduces the hydrogenation activation energy on the surface of Mg, thereby weakening the primary kinetic barrier of the absorption process. This effect resembles the shift in rate-limiting steps observed by Liu et al.[48] in $LaNi_5$-based systems, where the limiting mechanism changes from surface penetration to bulk diffusion. Furthermore, NbO_x reduced H doping energies (E_{doping}) by 0.25–0.37 eV, with NbO achieving the lowest value of −0.18 eV. By comparison, Nb_2 under the absence of oxygen demonstrates poor performance ($E_{ads} = -0.06$ eV) in terms of H atom migration during the hydrogenation process. Hence, it could be concluded that, under the support of graphene, Nb^{2+} and Nb^{4+} containing species exhibits best catalytic effect in promoting H_2 dissociation and diffusion into Mg and H_2 adsorption, respectively, and more importantly, both of them are major components of Nb_2O_5@G in situ formed during the hydrogen storage process of MgH_2 (Figure 3b). These results highlight the important synergistic role of multivalent Nb-based oxides in catalyzing the hydrogen absorption processes of Mg.

It is noteworthy that during the structural relaxation of the NbO_x@G system, the graphene substrate exhibited strong adsorptive behavior, particularly demonstrating pronounced affinity toward Nb atoms. This interfacial interaction could be quantitatively evidenced by the significant binding energy ($E_b < -1$ eV) between the NbO_x cluster and graphene, accompanied by a discernible outward displacement of oxygen-terminated edges as shown in Figure 5c. The hybridization between the *p* orbitals of C and the *d* orbitals of Nb, as shown in Figure S17 (Supporting Information), further indicates the significant confinement effect of graphene on both NbO_x species. This enables graphene to prevent the aggregation and crystallization of NbO_x clusters during cycling hydrogen storage, and hence the morphology of the Nb_2O_5@G-MgH_2 particles remained largely unchanged during cycling, as evidenced by the SEM images in Figure S18 (Supporting Information). The uniformly dispersed NbO_x species promote both nucleation and growth of the Mg/MgH_2 phase transition via a nanoconfinement-enhanced catalytic mechanism, as described by the extended Johnson–Mehl–Avrami–Kolmogorov (JMAK) model.[49,50] Overall, the unique electronic structure of multivalent Nb-based oxides supported on graphene significantly lowers the H_2 dissociation barrier and H adsorption energy on the NbO_x surface (Figure S19, Supporting Information), enabling facile hydrogen absorption at an ultralow temperature of 0 °C.

Interestingly, charge density difference analysis (Figure 5d) demonstrated that, under the support of graphene, graphene's π-electron contribution leads to the formation of the electron-rich regions at C-Nb interfaces (except for Nb_2). These regions likely create electron-accepting orbitals compatible with H_2 σ^* orbitals, significantly lowering the dissociation barrier, which in turn facilitates rapid H_2 cleavage (Figure S19, Supporting Information). In contrast, graphene also reduced the magnetic moment of Nb_2 from 2.0 μ_B to 0.0 μ_B (Figure 5c), eliminating spin-polarized states critical for charge transfer to H_2 σ^* antibonding orbitals, thereby increasing the H_2 dissociation barrier (Figure S14, Supporting Information). The spin-polarized *d* orbitals of Nb_2 cluster facilitate asymmetric electron transfer into H_2 σ^* antibonding orbital, thereby enhancing H—H bond cleavage via effective orbital hybridization (Figure S20, Supporting Information). Due to the strong hydrogen adsorption affinity (1.98 eV) of Nb, the dissociation of Nb—H bonds is hindered, leading to the formation of stable NbH_2 species, which subsequently impedes the migration of hydrogen into Mg. In this context, the reduced H_2 dissociation barrier of Nb^0 slows down the overall reaction on its surface, allowing more H_2 molecules to dissociate and adsorb on neighboring NbO_x species with lower H adsorption energies. This establishes a more efficient dissociation-diffusion pathway, rather than blocking H on Nb^0 sites via excessive NbH_2 formation. This mechanism is supported by the experimental observation in Figure 3b, where a significant reduction of Nb^0 is observed during hydrogenation in the absence of graphene, and the phase stability of Nb_2O_5@G after hydrogen absorption further confirms the transient yet rapid residence of hydrogen on the catalyst surface. Although partial NbH_2 formation still occurs due to the intrinsically low dissociation barrier of Nb (Figure 3c), the resulting NbH_2/MgH_2 interfacial structure forms a favorable gateway model during the subsequent dehydrogenation process, which effectively lowers the hydrogen adsorption barrier and hence promotes facile hydrogen storage of MgH_2 at room temperature.

3. Conclusion

In this study, we design and synthesize graphene-stabilized multivalent niobium oxide nanoparticles (Nb_2O_5@G) as a high-efficiency catalyst for promoting the hydrogen storage performance of MgH_2. During cycling hydrogen storage, MgH_2 under the catalysis of Nb_2O_5@G not only retains a stable hydrogen capacity of 6.3 wt.% but also achieves a reduction of the onset dehydrogenation temperature to 155.9 °C, which is 124.1 °C lower than that of pure MgH_2. In terms of reversible hydrogen absorption, MgH_2 instantaneously achieves a capacity of 5.0 wt.% within 1 min at ambient temperature (25 °C), and it retains 5.0 wt.% hydrogen uptake even at 0 °C, demonstrating unprecedented low-temperature hydrogen absorption capability. Both experimental and theoretical results revealed that Nb_2O_5 undergoes in situ reduction to low-valence niobium oxides (NbO_x) and elemental Nb during the hydrogenation/dehydrogenation process, where different Nb oxidation states play distinct catalytic roles. Specifically, in comparison with crystalline Nb_2O_5, all the thus-formed NbO_x clusters exhibit significantly superior hydrogenation and dehydrogenation performance due to their barrierless H_2 dissociation and the ability to lower the H adsorption energy on Mg surfaces from 0.01 to −0.99 eV. Meanwhile, NbO_2 facilitates hydrogen diffusion into Mg by reducing the interstitial doping energy from 0.19 to −0.19 eV. Notably, Graphene played an additional role in enhancing the catalytic effect of NbO_x, which ensures uniform dispersion of Nb_2O_5 within MgH_2 and prevents particle agglomeration of NbO_x and maintains intimate contact between NbO_x and MgH_2 during hydrogen absorption-desorption cycles. This tight interface facilitates the rapid

reduction of nanosized Nb_2O_5 on the MgH_2 surface, which significantly enhances catalytic activity for hydrogen absorption by mitigating the low efficiency of the saturated coordination state of Nb^{5+}. Moreover, the electron-rich regions formed at the interface between graphene and NbO_x effectively lower the H_2 dissociation barriers across all niobium oxide species, which, more importantly, simultaneously reduces the unpaired spin electrons of Nb^0 that would elevate the H_2 dissociation barrier at Nb^0 sites. Consequently, hydrogen stagnation by the strong Nb—H bonds is suppressed, facilitating efficient hydrogen migration into Mg and accelerating the overall hydrogen absorption kinetics. This work not only achieves a breakthrough in niobium-based catalytic performance for MgH_2 but also provides a comprehensive mechanistic framework for designing multivalent metal oxide catalysts in hydrogen storage systems.

4. Experimental Section

Materials and Preparation—Preparation of Nb_2O_5@G: To prepare Nb_2O_5@G, 100 mg of $NbCl_5$ (≥99.9%, Aladdin) was dissolved in 20 mL of anhydrous ethanol under stirring in an ice-water bath to form solution A. Separately, 6.4 mL of graphene oxide (GO) dispersion (2 mg mL^{-1}, Tanfeng Tech.Inc.) was ultrasonicated in 20 mL of anhydrous ethanol to produce solution B. Solution B was then gradually added to solution A, and the combined solution was stirred continuously in the ice-water bath while 1 mL of oleylamine (C18 content: 80–90%, Aladdin) was added dropwise. The mixture was then heated to 75 °C and stirred vigorously for 6 h. The resultant product was washed sequentially with ethanol and deionized water, followed by centrifugation. Subsequently, 120 mg of sodium ascorbate (≥99%, Aladdin) and 8 mL of deionized water were added to disperse the product by ultrasonication, and the mixture was heated at 100 °C for 2 h to reduce the graphene oxide. The sample was then washed with deionized water, centrifuged, and freeze-dried. The dried sample was placed in a tubular furnace and heated at a rate of 5 °C min^{-1} to 600 °C under a N_2 atmosphere. This temperature was maintained for 3 h, after which the sample was allowed to cool naturally to room temperature to obtain Nb_2O_5@G.

Materials and Preparation—Preparation of Nano-Nb_2O_5: The preparation of nano-Nb_2O_5 followed the same procedure as Nb_2O_5@G, with the exception that during the high-temperature calcination step, air rather than N_2 was introduced into the tubular furnace.

Materials and Preparation—Preparation of MgH_2-Nb_2O_5@G Composite: The MgH_2-Nb_2O_5@G composite was synthesized by high-energy ball milling, using a stainless-steel milling jar and balls capable of withstanding high pressure. The mass ratio of the milling balls to the sample was 120:1, and the rotation speed of the miller was maintained at 500 rpm (alternate clockwise and counterclockwise rotation) for 12 h (20 min stop every 10 min). The milling process was carried out under a 50 bar H_2 atmosphere within the jar. All sample preparations were conducted in an argon-filled glovebox, where both water and oxygen levels were maintained below 0.01 ppm. Control samples were prepared under the same milling parameters as MgH_2-Nb_2O_5@G.

Material Characterization: The phase composition of the powdered samples was analyzed using X-ray diffraction (XRD) on a Bruker D8 Advance diffractometer with Cu Kα radiation (λ = 1.5418 Å). To prevent air-induced reactions, all samples were covered with an amorphous tape, producing a broad peak around $2\theta = 20°$. Sample morphology was examined through field-emission scanning electron microscopy (FE-SEM, ZEISS Gemini 300) and transmission electron microscopy (TEM, FEI Tecnai F20). For surface analysis, X-ray photoelectron spectroscopy (XPS) was conducted with a ThermoFisher ESCALAB 250Xi, USA, under an analysis chamber pressure of 8×10^{-10} Pa, using an Al Kα excitation source ($h\nu$ = 1486.6 eV), with a working voltage of 12.5 kV, filament current of 16 mA, and signal accumulation over 5–10 cycles. Data were acquired with a pass energy of 20 eV and a step size of 0.1 eV. The Nb 3*d* region was calibrated using the sp^2-hybridized carbon peak of graphene at 284.0 eV to correct for charging effects, instead of the typical adventitious carbon peak at 284.8 eV, to ensure accuracy in binding energy referencing. For samples without graphene, the adventitious carbon peak was referenced at 284.8 eV. Peak fitting was performed using a Gaussian-Lorentzian mixed function with an L/G ratio of 30%. The spin-orbit doublets ($3d_{5/2}$ and $3d_{3/2}$) were constrained with an area ratio of 3:2 and a fixed energy separation of 2.8 ± 0.1 eV. The full width at half maximum (FWHM) was maintained consistently within each valence state: ≈0.9–1.0 eV for Nb^0, ≈1.7–1.8 eV for Nb^{2+}, and ≈1.9–2.0 eV for both Nb^{4+} and Nb^{5+}. Binding energy positions were referenced to established literature values. The content of each oxidation state was quantified by integrating the fitted peak areas and normalizing them to the total Nb 3*d* signal. Additionally, XPS spectra of the ball-milled sample were also analyzed to assess changes in Nb valence states after mechanical processing. Air-sensitive MgH_2 composites were transferred using a specially designed vessel in a glovebox to ensure no air contamination. Chemical bonding was analyzed via Fourier-transform infrared spectroscopy (FT-IR, Magna-IR 550 II, Nicolet), using KBr-pelletized powder samples compressed into translucent chips.

Hydrogen Storage Measurements: Hydrogen desorption and absorption properties of the prepared samples were measured through temperature-programmed desorption (TPD) and isothermal dehydrogenation, using a custom-built high-pressure sorption apparatus (HPSA), calibrated with $LaNi_5$ for hydrogen capacity accuracy within ±1%. Hydrogen storage capacity (wt.%) calculations were based on the total mass of each sample. Approximately 20 mg of each sample was used in these tests. TPD analyses were performed with a heating rate of 2 °C min^{-1}, while both TPD and isothermal dehydrogenation tests were carried out under an initial vacuum pressure of <0.0001 bar. The cycling stability was tested at 250 °C under isothermal conditions, with hydrogenation conducted at an initial pressure of 5 MPa.

Density functional theory calculation method: The Vienna Ab initio Simulation Package (VASP) was utilized to conduct spin-polarized density functional theory (DFT) calculations. Post-processing and analysis of VASP data were carried out using VASPKIT.[51] To accurately describe hydrogen absorption and desorption processes, the study employed the Perdew-Burke-Ernzerhof (PBE) functional within the generalized gradient approximation (GGA) framework, selected due to its reliable performance in prior benchmarking studies.[42,52,53] To address van der Waals forces in layered and cluster systems, the DFT-D3 dispersion correction method with Becke-Jonson damping was implemented.[54] Spin-polarized density functional theory calculations were performed to account for the possible magnetic behavior of the system, particularly in the presence of transition metal species and adsorbed hydrogen. The local magnetic moments on selected atoms were analyzed based on site-projected wavefunction data, enabling the characterization of spin states and their influence on the hydrogen adsorption mechanism.

For graphene-supported systems, the Nb_2 and NbO_x clusters were placed on a 4 × 4 graphene supercell (a = b = 9.87 Å) with a 20 Å vacuum layer along the c-axis, while isolated clusters were centered in a carbon-free box with equivalent vacuum spacing. MgH_2 (110) and Mg (001) substrates were modeled using 3 × 4 and 4 × 4 supercells, respectively, both with 25 Å vacuum layers. All calculations employed a 450 eV plane-wave cutoff, 0.05 eV Gaussian smearing, and DFT-D3 van der Waals correction. Slab systems used 4 × 4 × 1 *k*-point grids, whereas clusters were treated with Γ-point sampling. Electronic and ionic convergence criteria were set to 1×10^{-5} eV and 0.02 eV $Å^{-1}$, respectively. Transition states were rigorously determined using the climbing-image nudged elastic band (CI-NEB)[55] method combined with the improved dimer method (IDM),[56] ensuring higher accuracy than conventional nudged elastic band (NEB) approaches. For each CI-NEB calculation, 6–8 intermediate images were employed between the initial and final states to ensure a smooth transition along the reaction pathway. The average total atomic displacement between adjacent images was kept within 0.8 Å in the initial interpolation, guaranteeing a physically reasonable and continuous reaction coordinate. In this study, the Gibbs free energy was used for analysis (by considering

the entropic change and zero-point energy). The Gibbs free energies were calculated as follows:

$$G = E_e + E_{ZPE} - TS \quad (1)$$

where G represents the Gibbs free energy, E_e represents the DFT calculated energy, E_{ZPE} represents the zero-point energy, T represents the temperature, and S represents the entropic.

Meanwhile, multiple energy parameters were employed in theoretical calculations to evaluate the interactions between graphene, niobium oxide, Mg, and H, including the binding energy between graphene and NbO_x clusters (E_b), hydrogen adsorption energy (E_{ads}), and hydrogen dissociation energy (E_d). The computational methods used are as follows:

$$E_b = E_{total} - \left(E_{graphene} + E_{cluster}\right) \quad (2)$$

$$E_{ads} = E_{total} - (E_{substrate} + 1/2E_{H2}) \quad (3)$$

$$E_d = E_{2H*} - (E_{substrate} + E_{H2}) \quad (4)$$

where E_{total} represents the energy of the relaxed composite structure. $E_{graphene}$, $E_{cluster}$, $E_{substrate}$, E_{H2}, and E_{2H*} denote the energies of pristine graphene, free cluster, substrate for adsorption, isolated H_2 molecule, and the system with two adsorbed H atoms on the substrate, respectively.

Supporting Information

Supporting Information is available from the Wiley Online Library or from the author.

Acknowledgements

This work was partially supported by the National Natural Science Foundation of China (No. U2130208 and 22279020), and the Science and Technology Commission of Shanghai Municipality (No. 22ZR1406500 and 23ZR1406500).

Conflict of Interest

The authors declare no conflict of interest.

Data Availability Statement

The data that support the findings of this study are available in the supplementary material of this article.

Keywords

kinetic optimization, low-temperature hydrogenation, magnesium hydride, multivalent, niobium oxide nanoparticles

Received: June 19, 2025
Revised: July 30, 2025
Published online:

[1] L. Schlapbach, A. Züttel, *Nature* **2001**, *414*, 353.
[2] U. Eberle, M. Felderhoff, F. Schueth, *Angew. Chem., Int. Ed.* **2009**, *40*, 6608.
[3] A. Züttel, *Mater. Today* **2003**, *6*, 457.
[4] S. Niaz, T. Manzoor, A. H. Pandith, *Renewable Sustainable Energy Rev.* **2015**, *50*, 24.
[5] D. Pukazhselvan, V. Kumar, S. K. Singh, *Nano Energy* **2012**, *1*, 566.
[6] F. Schüth, B. Bogdanović, M. Felderhoff, *Chem. Commun.* **2004**, 2249.
[7] W. Grochala, P. P. Edwards, *Chem. Rev.* **2004**, *104*, 1283.
[8] N. S. Norberg, T. S. Arthur, S. J. Fredrick, A. L. Prieto, *J. Am. Chem. Soc.* **2011**, *133*, 10679.
[9] B. Bogdanović, A. Ritter, B. Spliethoff, *Angewandte Chemie International Edition in English* **1990**, *29*, 223.
[10] G. Liang, J. Huot, S. Boily, R. Schulz, *J. Alloys Compd.* **2000**, *305*, 239.
[11] Y. Xinglin, L. Xiaohui, Z. Jiaqi, H. Quanhui, Z. Junhu, *Mater. Today Adv.* **2023**, *19*, 100387.
[12] Y. Zhang, S. Wu, L. Wang, X. Zhang, *Frontiers in Energy* **2023**, *17*, 72.
[13] Z. Han, Y. Wu, H. Yu, S. Zhou, *J. Magnesium Alloys* **2022**, *10*, 1617.
[14] M. Pozzo, D. Alfe, *Int. J. Hydrogen Energy* **2009**, *34*, 1922.
[15] K. Takahashi, S. Isobe, S. Ohnuki, *Langmuir* **2013**, *29*, 12059.
[16] G. Barkhordarian, T. Klassen, R. Bormann, *Scr. Mater.* **2003**, *49*, 213.
[17] G. Barkhordarian, T. Klassen, R. Bormann, *J. Phys. Chem. B* **2006**, *110*, 11020.
[18] H. Hirate, Y. Saito, I. Nakaya, H. Sawai, Y. Shinzato, H. Yukawa, M. Morinaga, T. Baba, H. Nakai, *Int. J. Quantum Chem.* **2009**, *109*, 2793.
[19] O. Friedrichs, J. C. Sánchez-López, C. López-Cartes, T. Klassen, R. Bormann, A. Fernández, *J. Phys. Chem. B* **2006**, *110*, 7845.
[20] K. Takahashi, S. Isobe, S. Ohnuki, *J. Alloys Compd.* **2013**, *580*, S25.
[21] Y. Sun, C. Shen, Q. Lai, W. Liu, D.-W. Wang, K.-F. Aguey-Zinsou, *Energy Storage Mater.* **2018**, *10*, 168.
[22] Q. Li, M. Yan, Y. Xu, X. L.i Zhang, K. T. Lau, C. Sun, B. Jia, *J. Phys. Chem. C* **2021**, *125*, 8862.
[23] K. Kajiwara, H. Sugime, S. Noda, N. Hanada, *J. Alloys Compd.* **2022**, *893*, 162206
[24] M. O. T. da Conceição, M. C. Brum, D. S. dos Santos, M. L. Dias, *J. Alloys Compd.* **2013**, *550*, 179.
[25] H. Guan, Y. Lu, J. Liu, Y. Ye, Q. Li, F. Pan, *ACS Catal.* **2024**, *14*, 17159.
[26] H. Guan, J. Liu, X. Sun, Y. Lu, H. Wang, Q. Luo, Q. Li, F. Pan, *Adv. Mater.* **2025**, *37*, 2500178.
[27] R. Zou, J. Li, W. Zhang, G. Lei, Z. Li, H. Cao, *J. Mater. Chem. A* **2023**, *11*, 11748.
[28] S. Tamura, K. Kato, M. Goto, *Zeitschrift fur Anorganische und Allgemeine Chemie* **1974**, *410*, 313.
[29] P. Carniti, A. Gervasini, M. Marzo, *J. Phys. Chem. C* **2008**, *112*, 14064.
[30] Y. Meng, J. Zhang, S. Ju, Y. Yang, Z. Li, F. Fang, D. Sun, G. Xia, H. Pan, X. Yu, *J. Mater. Chem. A* **2023**, *11*, 9762.
[31] X. Zhang, K. Wang, X. Zhang, J. Hu, M. Gao, H. Pan, Y. Liu, *Int. J. Energy Res.* **2021**, *45*, 3129.
[32] H. Liu, C. Lu, X. Wang, L. Xu, X. Huang, H. Ning, Z. Lan, J. Guo, *ACS Appl. Mater. Interfaces* **2021**, *13*, 133985.
[33] Z. Lan, H. Fu, R. Zhao, H. Liu, W. Zhou, H. Ning, J. Guo, *Chem. Eng. J.* **2022**, *431*, 13235.
[34] X. Zhang, X. Zhang, L. Zhang, Z. Huang, L. Yang, M. Gao, C. Gu, W. Sun, H. Pan, Y. Liu, *ACS Appl. Nano Mater.* **2023**, *6*, 14527.
[35] C. Peng, X. Chen, Q. Zhang, *J. Alloys Compd.* **2025**, 178709.
[36] W. Shi, F. Hong, R. Li, R. Zhao, S. Ding, Z. Liu, P. Qing, Y. Fan, H. Liu, J. Guo, Z. Lan, *J. Energy Storage* **2023**, *72*, 108738.
[37] J. A. Bolarin, Z. Zhang, H. Cao, Z. Li, T. He, P. Chen, *J. Magnesium Alloys* **2023**, *11*, 2740.
[38] D. Chen, Y. M. Wang, L. Chen, S. Liu, C. X. Ma, L. B. Wang, *Acta Mater.* **2004**, *52*, 521.
[39] T. Noritake, M. Aoki, S. Towata, Y. Seno, Y. Hirose, E. Nishibori, M. Takata, M. Sakata, *Appl. Phys. Lett.* **2002**, *81*, 2008.
[40] Y.i Jia, C. Sun, L. Cheng, M.d Abdul Wahab, J. Cui, J. Zou, M. Zhu, X. Yao, *Phys. Chem. Chem. Phys.* **2013**, *15*, 5814.
[41] M. Tsuda, W. A. Diño, H. Kasai, H. Nakanishi, H. Aikawa, *Thin Solid Films* **2006**, *509*, 157.

[42] C. Li, W. Yang, H. Liu, X. Liu, X. Xing, Z. Gao, S. Dong, H. Li, *Angew. Chem., Int. Ed.* **2024**, *63*, 202320151.
[43] S. Dong, C. Li, J. Wang, H. Liu, Z. Ding, Z. Gao, W. Yang, W. Lv, L.i Wei, Y. Wu, H. Li, *J. Mater. Chem. A* **2022**, *10*, 22363.
[44] E. M. Kumar, A. Rajkamal, R. Thapa, *Sci. Rep.* **2017**, *7*, 15550.
[45] G. Wu, J. Zhang, Q. Li, Y. Wu, K. Chou, X. Bao, *Comput. Mater. Sci.* **2010**, *49*, S144.
[46] D. Khan, J. Zou, S. Panda, W. Ding, *J. Phys. Chem. C* **2020**, *124*, 9685.
[47] J. Lyu, V. Kudiiarov, L. Svyatkin, A. Lider, K. Dai, *Catalysts* **2023**, *13*, 519.
[48] J. Liu, X. Zhang, Q. Li, K.-C. Chou, K.-D. Xu, *Int. J. Hydrogen Energy* **2009**, *34*, 1951.
[49] Y. Pang, D. Sun, Q. Gu, K.-C. Chou, X. Wang, Q. Li, *Cryst. Growth Des.* **2016**, *16*, 171.
[50] Q. Luo, Y. Guo, B. Liu, Y. Feng, J. Zhang, Q. Li, *J. Mater. Sci. Technol.* **2020**, *44*, 2404.
[51] V. Wang, N. Xu, J.-C. Liu, G. Tang, W.-T. Geng, *Comput. Phys. Commun.* **2021**, *267*, 108033.
[52] J. Wellendorff, T. L. Silbaugh, D. Garcia-Pintos, J. K. Nørskov, T. Bligaard, F. Studt, C. T. Campbell, *Surf. Sci.* **2015**, *640*, 36.
[53] J. P. Perdew, K. Burke, M. Ernzerhof, *Phys. Rev. Lett.* **1996**, *77*, 3865.
[54] S. Grimme, J. Antony, S. Ehrlich, H. Krieg, *J. Chem. Phys.* **2010**, *132*, 154104.
[55] G. Henkelman, B. P. Uberuaga, H. Jónsson, *J. Chem. Phys.* **2000**, *113*, 9901.
[56] G. Henkelman, H. Jónsson, *J. Chem. Phys.* **1999**, *111*, 7010,